Mechanism of high-resolution STM/AFM imaging with functionalized tips

Prokop Hapala[*]

Institute of Physics, Academy of Sciences of the Czech Republic, v.v.i., Cukrovarnická 10, 162 00 Prague, Czech Republic

Georgy Kichin, Christian Wagner, F. Stefan Tautz, and Ruslan Temirov[†]

Peter Grünberg Institut (PGI-3), Forschungszentrum Jülich, 52425 Jülich, Germany
and Jülich Aachen Research Alliance (JARA), Fundamentals of Future Information Technology, 52425 Jülich, Germany

Pavel Jelínek[‡]

Institute of Physics, Academy of Sciences of the Czech Republic, v.v.i., Cukrovarnická 10, 162 00 Prague, Czech Republic
and Graduate School of Engineering, Osaka University 2-1, Yamada-Oka, Suita, Osaka 565-0871, Japan
(Received 16 June 2014; revised manuscript received 23 July 2014; published 19 August 2014)

High-resolution atomic force microscopy (AFM) and scanning tunneling microscopy (STM) imaging with functionalized tips is well established, but a detailed understanding of the imaging mechanism is still missing. We present a numerical STM/AFM model, which takes into account the relaxation of the probe due to the tip-sample interaction. We demonstrate that the model is able to reproduce very well not only the experimental intra- and intermolecular contrasts, but also their evolution upon tip approach. At close distances, the simulations unveil a significant probe particle relaxation towards local minima of the interaction potential. This effect is responsible for the sharp submolecular resolution observed in AFM/STM experiments. In addition, we demonstrate that sharp apparent intermolecular bonds should not be interpreted as true hydrogen bonds, in the sense of representing areas of increased electron density. Instead, they represent the ridge between two minima of the potential energy landscape due to neighboring atoms.

PACS number(s): 68.37.Ef, 68.37.Ps, 82.30.Rs, 68.49.Df

I. INTRODUCTION

Scanning tunneling microscopy (STM) [1] and atomic force microscopy (AFM) [2] methods are key tools of nanoscience. One of their most remarkable achievement is the unprecedented submolecular resolution of both atomic and electronic structures of single molecules on surfaces. First real space images of molecular orbitals were obtained with STM [3]. Then it was found that functionalizing the tip with a single carbon monoxide (CO) molecule enhances the resolution of molecular orbital STM images [4,5]. Later it has been discovered that STM tip functionalization with H_2, D_2 [so-called scanning tunneling hydrogen microscopy (STHM) [6,7]] and a variety of other atomic and molecular particles (Xe, CH_4, CO) allows the STM to resolve the *atomic* structures of large organic adsorbates in a direct imaging experiment [6–9]. Finally, the development of the qPlus AFM technique [10] has resulted in the successful resolution of internal molecular structures by AFM [11,12].

On the basis of a density functional theory (DFT) analysis the high resolution of molecular structures in AFM has been attributed to Pauli repulsion [11,13]. Following this result it has been proposed that the contrast delivered by functionalized STM tips is related to the same force [7]. Several groups have also pointed out the influence of CO-tip bending on the distortion that is present in high-resolution AFM images [12,14,15].

One peculiar feature of the high-resolution STM/AFM images obtained with functionalized tips, namely the striking imaging contrast obtained in areas between molecules [8,9,16,17], has, however, not yet been clearly explained. In particular, the sharp ridges observed in the high-resolution images do not necessarily represent a true bond. For example, Pavlicek *et al.* [18] observed in high-resolution images of DBTH molecules an apparent bond ridge between sulfur atoms where there is no chemical bond.

Very recently it has been argued that sharp contrast features between the molecules may be related to the imaging of hydrogen bonds [17], as a consequence of an enhanced electron density between oxygen and hydrogen atoms of neighboring molecules. But it is not clear why in experiment this contrast appears so sharp, especially since according to DFT simulations the electron density variation is expected to be exceedingly small [17]. The sharp lines visible in these experiments therefore cannot be automatically ascribed to (hydrogen) bonds. This calls for a deeper understanding of the origin of the high-resolution contrast in general.

In this work we propose a simple mechanical model of the functionalized STM/AFM junction that clarifies all of the main features of STM and AFM images measured with functionalized tips. First, it explains the appearance of characteristic sharp features in STM and AFM images measured at close tip-sample distances. Secondly, it establishes the relationship between the observed AFM and STM image contrasts obtained with functionalized tips. Thirdly, it reveals the nature of the STM and AFM contrasts in the intermolecular regions and allows a critical discussion of the appearance of so-called hydrogen bonds in the images. Finally, the method allows us to simulate AFM/STM images of complete molecular layers at different tip-sample distances at small

---
[*]Corresponding author: hapala@fzu.cz
[†]r.temirov@fz-juelich.de
[‡]pavel.jelinek@fzu.cz

computational cost. To underpin the predictive power of our model, we compare AFM/STM images obtained from our numerical model to selected experimental cases.

II. METHODS

A. Equipment and sample preparation

The experiments were performed using a combined NC-AFM/STM from Createc. The base pressure at the working temperature of 5 K was better than 10^{-11} mbar. All samples were prepared using standard techniques of surface preparation in ultrahigh vacuum. Submonolayer coverages of PTCDA were deposited onto freshly prepared surfaces of Au(111) and Ag(111) at room temperature using a homebuilt Knudsen cell. Immediately after the deposition the sample was transferred to the cold (5 K) STM. Individual xenon atoms and carbon monoxide molecules were deposited onto the sample at 5 K by closing the ion getter pump, opening the shutter in the cryoshields, and flooding the STM chamber with the clean gas for 10 min at a pressure of about 5×10^{-9} mbar. The tip decoration was effected according to the procedures described in Ref. [8].

B. Preparation molecular geometry for simulation

The molecular geometry of PTCDA monolayers on the respective metallic substrates was determined from supercell parameters obtained from Ref. [19] in the case of Au(111) and from Ref. [20] for Ag(110). Atomic coordinates for the 8-hydroxyquinoline tetramer were taken from Ref. [17]. The molecular geometries were then relaxed in the relevant supercell using the local orbital DFT code FIREBALL [21,22] within the local-density approximation (LDA) for the exchange-correlation functional. During the relaxation the molecular geometry was free to move in the x, y plane, while the z coordinates of all atoms were set to $z = 0$ and fixed. Convergence was achieved once a residual total energy of 0.0001 eV and a maximal force of 0.05 eV/Å were reached. The atomic structure of NTCDI molecules on Ag:Si(111)-$(\sqrt{3} \times \sqrt{3})$ was taken from DFT calculations published in Ref. [23] (see Fig. 3.C of that reference).

C. Mechanical AFM model

The main ingredient of our model is the geometric distortion of the "soft" apex of a functionalized tip due to the interaction with the surface [12]. We model this soft apex as the outermost atom of the metal tip (*tip base*) and the *probe particle* that decorates it (see Fig. 1).

To account for the interaction between the functionalized tip and a molecular layer ("sample") on the surface we construct a force-field model of the junction using empirical potentials. In particular, we use a pairwise Lennard-Jones (LJ) potential to describe the weak interaction F_{Surf} between the probe particle of the functionalized tip and the sample (see Fig. 1). F_{Surf} is calculated as a sum of all pairwise LJ forces acting between the probe particle and the atoms constituting the molecular layer. Besides F_{Surf} the probe particle experiences two additional forces: (i) a radial LJ force $F_{Tip,R}$ between the probe particle and the tip base which keeps the probe particle attached to
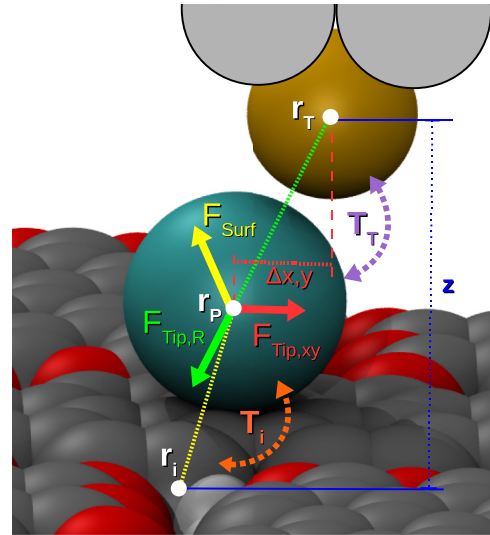

FIG. 1. (Color online) AFM/STM model. Schematic view of the mechanical model of a functionalized tip as employed in this work. The last metal atom of the tip (*tip base*) is shown in sand color, the probe particle in cyan, and the molecular layer (*sample*, in the example a herringbone PTCDA layer) in gray (carbon atoms) and red (oxygen atoms). The forces acting on the probe particle are shown in color: radial tip force $F_{Tip,R}$ (green); lateral tip force $F_{Tip,xy}$ (red); force F_{Surf} exerted by atoms of the sample (yellow). Force-determining geometric parameters are shown in the same color as the corresponding forces. The two distinct hopping processes in our STM model are denoted by violet (probe particle tip, T_T) and orange (probe particle sample, T_i) color. The reference distance z that is used throughout the paper is shown in blue.

the tip base at a particular distance and (ii) an additional lateral harmonic force $F_{Tip,xy}$ that stems from the cylindrically symmetric attractive potential of the tip base.

In this work we employ two different sets of LJ parameters (binding energy ϵ_α and equilibrium distance r_α) of the $F_{Tip,R}$ interaction to mimic Xe- and CO-decorated tips (cf. Supplemental Material [25], Table 1), while the lateral stiffness $k_{xy} = 0.5$ N/m is kept constant for all types of probe particles. Interestingly, we find that the results depend only weakly on variations of the binding energy parameter ϵ_α (cf. Supplemental Material [25], Fig. 1). This observation agrees well with the fact that the high-resolution images of a particular molecule obtained with different functionalized tips look qualitatively similar [26]. It turns out that the variation of the image contrast between different probe particles is mainly related to their different van der Waals radii, in our model defined by r_α (cf. Supplemental Material [25], Fig. 2). The Lennard-Jones parameters used in the mechanical model of probe particle relaxation for H, C, O, and Xe atoms were taken from the OPLS force field [24] (for more details, see Supplemental Material [25], Table 1 and methods). The robustness of the simulations with respect to the precise values of these parameters is demonstrated in the Supplemental Material [25], Figs. 1–3. Regarding the procedure with which the simulated AFM images were generated, refer to methods in Supplemental Material [25].
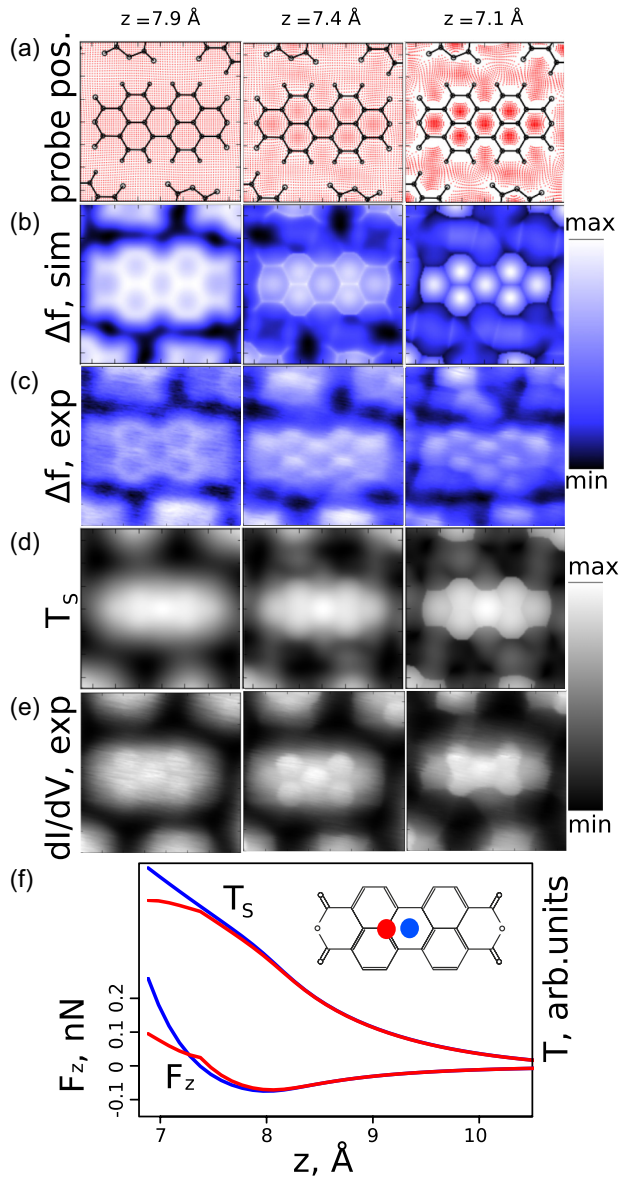
FIG. 2. (Color online) Simulated and experimental high-resolution AFM and STM images. Experimental images have been recorded on PTCDA/Au(111) with a CO probe particle. Simulated images have been obtained with LJ parameters mimicking the oxygen atom of CO. (a) Map of simulated probe particle positions after relaxation. (b) Simulated AFM image (the frequency shift Δf is displayed). (c) Experimental AFM images (frequency shift). (d) Simulated STM images (maps of the T_S tunneling process). (e) Experimental STM images (differential conductance). (f) Vertical force F_z (left axis) and tunneling probability T_S (right axis, arbitrary units), both as a function of tip-sample distance z, computed over different sites of the sample as indicated by the red and blue dots in the PTCDA structure formula. Experimental images in panels (c) and (e) are taken from Ref. [9]). All simulated images except (a) are normalized to obtain maximum contrast.

We use our model to simulate the images of the well-known herringbone monolayer of 3,4,9,10-perylene tetracarboxylic dianhydride (PTCDA). PTCDA layers, as well as single PTCDA molecules, have been extensively imaged with functionalized STM/AFM tips [6–9,16,27]. Therefore, a wealth of
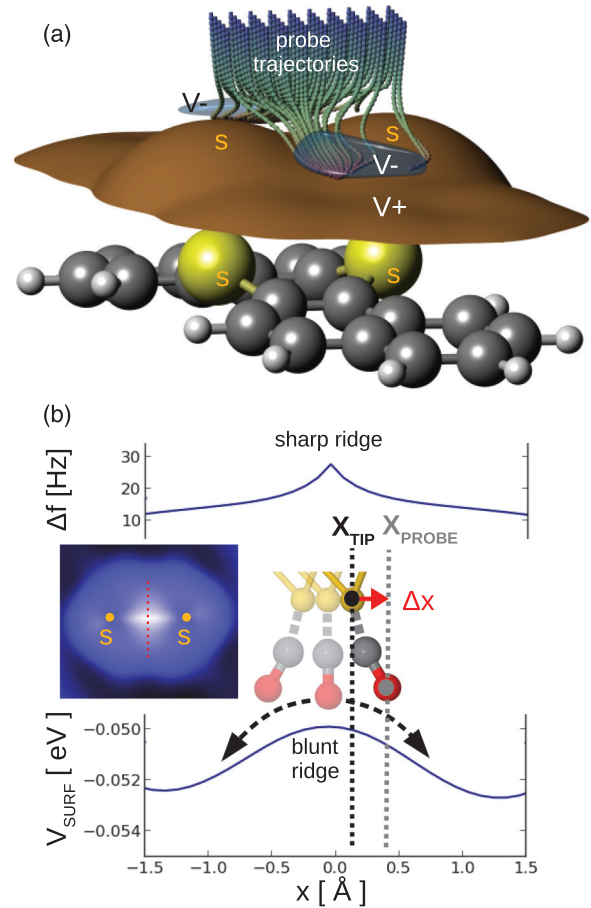

FIG. 3. (Color online) Origin of sharp lines in AFM images. (a) DBTH molecule (sulfur atoms in yellow, carbon atoms in dark gray, and hydrogen atoms in light gray), with repulsive potential felt by the probe particle in brown ($V+$) and attractive basins ($V-$) in blue. Probe particle trajectories upon tip approach are also shown. Sulfur-derived hillocks in the repulsive potential are labeled "S." Between them, a repulsive saddle is formed. (b) Surface potential V^{Surf} (bottom) and AFM frequency shift Δf (top) along the central cross section of the repulsive saddle. In the center the relaxation Δx of the probe particle towards the position x_{probe} is shown schematically for a tip position x_{tip} close to the ridge of the saddle. The mapping of the force at x_{probe} to the macroscopic tip position x_{tip} explains the sharpening of the Δf curve ("sharp ridge") even for a smooth saddle in V^{Surf} ("blunt ridge"). The inset shows a simulated AFM image of DBTH in the region of the two sulfur atom, clearly exhibiting the sharp line between the two sulfur atoms.

experimental data is readily available for direct comparison to the results of our simulations. As mentioned above, the input atomic structure of the molecular layer was taken from the data published for PTCDA/Au(111) [19], and the structure was further optimized with DFT.

The simulated data were acquired by scanning the model tip laterally over the surface with a step of $\Delta x, \Delta y = 0.1$ Å. At each lateral position, the tip was placed at an initial set point $z_0 = 12$ Å above the molecular layer (cf. Fig. 1 for the definition of the z coordinate). Subsequently, we approached the tip vertically towards the sample in steps of $\Delta z = 0.1$ Å until $z = 6$ Å. At each step of the vertical approach the probe particle position was allowed to relax until the net force

$F_{Surf} + F_{Tip,R} + F_{Tip,xy}$ acting on the probe particle (see Fig. 1) became smaller than 10^{-6} eV/Å. At the same time the degrees of freedom of the molecular layer and the tip base were kept fixed. Once the structural relaxation was completed, the vertical force F_z was calculated from a projection of F_{Surf} onto the z axis. Finally, the $F_z(z)$ curves were converted to frequency shift $\Delta f(z)$ using the inverse Sader formula [28]. We note that in our experiments the qPlus sensor was oscillating with a very small amplitude (0.2 Å from zero to peak). The same value was used in our numerical simulations.

D. STM model

On top of the mechanical AFM model we derive a simple numerical model for STM simulations, the main objective of which is to understand the variation of the tunneling current as a function of probe particle relaxation. The model is based on Landauer theory [29]. We start from the Landauer formula for the conductance $dI/dV(\epsilon) = \frac{2e}{h}\Gamma_T(\epsilon)G_P^\dagger(\epsilon)\Gamma_S(\epsilon)G_P(\epsilon)$, where $G_P(\epsilon)$ is the Green's function of the probe particle at energy ϵ and $\Gamma_{T,S}(\epsilon) = 2\,\mathrm{Im}\Sigma_{T,S}(\epsilon)$, where the $\Sigma_{T,S}(\epsilon) = t_{T,S}^\dagger G_{T,S}t_{T,S}$ represent the self-energies of tip (T) and sample (S), respectively; the $t_{T,S}$ quantify the hopping between the probe particle and tip or sample, respectively. To simplify our model we adopt several approximations. (i) We are interested just in the conductance at zero bias voltage, so we set $\epsilon = \epsilon_F$, where ϵ_F is the Fermi energy. (ii) We neglect the real part of the probe particle Green's function, i.e., $\mathrm{Re}G_P(\epsilon_F) \approx 0$, and we express the local density of states (LDOS) of the probe particle as $\rho_P(\epsilon_F) = \frac{1}{\pi}\mathrm{Im}G_P(\epsilon_F)$. In a similar way, we can also rewrite $\Gamma_{T,S}(\epsilon_F) \approx t_{T,S}^\dagger(\epsilon_F)\rho_{T,S}(\epsilon_F)t_{T,S}(\epsilon_F)$, where $\rho_{T,S}(\epsilon_F) = \frac{1}{\pi}\mathrm{Im}G_{T,S}(\epsilon_F)$ denote the LDOS of tip and sample, respectively. (iii) We consider all tunneling channels between the probe particle and individual atoms of the sample as independent. Thus we can write $\Gamma_S = \sum_i \Gamma_i$, where $\Gamma_i = t_i^\dagger \rho_i(\epsilon_F)t_i$ is the electronic coupling of the ith atom of the sample to the probe particle (see Fig. 1). (iv) We assume that the sample LDOS $\rho_{T,S}(\epsilon)$ is spread homogeneously over all carbon and oxygen atoms of the molecules which make up the sample, i.e., the LDOS $\rho_i(\epsilon_F)$ of all atoms is the same ($\rho_i^{C,O} = $ const). (v) Neither hydrogen atoms of the molecules nor atoms of the metallic substrate are considered. Disregarding the hydrogen atoms is motivated by the fact that the frontier orbitals of large aromatic molecules such as PTCDA are localized mostly on the carbon backbone and on substituents with free electron pairs, while their amplitude on the peripheral hydrogen atoms is negligible (see, e.g., Ref. [30]). (vi) Finally we assume all LDOS [$\rho_P(\epsilon_F)$, $\rho_T(\epsilon_F)$, $\rho_i(\epsilon_F)$] to remain constant during the scanning process. Therefore, they are just multiplicative constants which do not affect the tunneling current variation along the tip trajectory. Consequently, the conductance is only a function of the positions of the tip base atom $\vec{r}_T$, surface atoms $\vec{R}_S$ ($\vec{r}_i$ for individual atoms), and the probe particle $\vec{r}_P$:

$$dI/dV(\vec{r}_P,\vec{r}_T,\vec{R}_S) \propto T_T(\vec{r}_P,\vec{r}_T)T_S(\vec{r}_P,\vec{R}_S)$$
$$= T_T(\vec{r}_P,\vec{r}_T)\sum_i T_i(\vec{r}_P,\vec{r}_i). \quad (1)$$

In other words, we can describe the conductance through the probe particle junction via two terms: (a) tunneling

from the tip to the probe particle ($T_T \approx t_T^\dagger t_T$) and (b) subsequent tunneling from the probe particle to the sample ($T_S \approx \sum_i T_i = \sum_i t_i^\dagger t_i$) (see Fig. 1). The tunneling process T_i between a given sample atom and the probe particle can be expressed as an exponential function $T_i \propto \exp(-\beta_S|\vec{r}_P - \vec{r}_i|)$, where β_S represents the characteristic decay length of the tunneling process between the probe particle and sample atom i. Similarly, we can define $T_T \propto \exp(-\beta_T|\vec{r}_P - \vec{r}_T|)$. An angular momentum dependence of the hopping can also be included (cf. Supplemental Material [25] methods and Fig. 5). Because we are only interested in the variation of the atomic STM contrast due to the probe particle relaxation, we consider for simplicity both characteristic decay lengths β to be independent of the tip-sample distance and equal $\beta_S = \beta_T = 1\text{Å}^{-1}$. We can plot maps of the tunneling processes T_S and T_T separately to analyze the effects of tip-probe and sample-probe relaxation qualitatively and irrespective of the sizes of the two β. In reality, β_S and β_T may differ from each other and according to Eq. (1) their relative sizes will influence the relative impact of T_S and T_T on the conductance image.

Clearly, our numerical model omits many processes that happen during tip-sample interaction (e.g., variations of the LDOS or the tunneling barrier, multiple scattering effects, etc. [31]). Moreover, at close tip-sample proximity additional mechanical degrees of freedom of the junction, such as relaxations inside the tip, within the molecular layer and the surface, will eventually become important. Nevertheless, as will be demonstrated here, this simple model accounts for most of the observed contrast features, which proves the crucial importance of probe particle relaxation also for the high-resolution STM contrast.

III. RESULTS AND DISCUSSION

A. High-resolution AFM contrast: Inversion and sharpening

We start the discussion by showing the equilibrium position of the probe particle when a model tip decorated by CO ("CO tip") is scanned over PTCDA molecules in the herringbone monolayer. Figure 2(a) clearly shows that at closer distances the functionalized tip experiences sidewise relaxation. The observed lateral relaxations are induced by the Pauli repulsion that acts at short distances between the probe particle and the atoms of the PTCDA layer: the probe particle tends to relax away from the areas where the Pauli repulsion is strong. According to Fig. 2(a), the Pauli repulsion potential over the PTCDA forms "basins" which become clearly visible as the tip approaches the sample.

Let us now inspect the effect that the tip relaxation has on the frequency shift Δf. The maps of Δf in Fig. 2(b), calculated at the same tip-sample distances as Fig. 2(a), clearly show the *inversion* of the Δf contrast when the tip approaches the sample. Since the observed evolution of the simulated Δf images closely matches the experiment [see Fig. 2(c)], we can identify the mechanism that drives the experimentally observed inversion of the Δf image contrast by analyzing the calculated $F_z(z)$ curves shown in Fig. 2(f).

The two $F_z(z)$ curves calculated for the tip approach over the carbon atom (red) and over the center of the aromatic ring (blue) clearly show that initially the repulsion over the carbon

atom increases faster upon tip approach. The situation changes at the distance $z \approx 7.4$Å [Fig. 2(f)] when the probe particle starts to move laterally in order to minimize the effect of the increasing repulsive force. Finally, the repulsion over the ring center becomes stronger, because there the tip is located in the middle of a potential basin that hinders lateral relaxations of the probe particle and thus prevents the relief of the repulsive force.

Comparing the simulated force curves in Fig. 2(f) with corresponding experimental ones reported in Ref. [9], we find that both exhibit a very similar behavior. Small differences between the published experimental $F_z(z)$ curves and the simulated ones shown here can be explained by two facts. First, in our present simulations we do not take into account the attractive interaction between the metal atoms of the tip and the sample. That results in the absence of the attractive force that appears in the experiment after the probe particle has relaxed laterally out of the junction. Secondly, in the simulation we position the tip precisely over the carbon atom and do not take into account the finite amplitude of the qPlus oscillation. This produces a sharp kink in $F_z(z)$ at the moment when the probe particle starts relaxing laterally at the distance $z \approx 7.4$Å [see Fig. 2(f)]. Despite these small and well-understood discrepancies between the experimental and simulated force curves the overall good agreement between both allows us to conclude that the Δf inversion observed both in experiments and simulations occurs due to the decrease of the repulsive force produced by the lateral relaxation of the probe particle in the junction.

Having shown that our model captures the Δf inversion correctly, we note that the inversion effect develops together with a considerable *sharpening* of various features in the Δf images [see the middle and the right panels of Fig. 2(b) and Supplemental Material [25], Video 1]. Hence the evident sharpening of the experimental Δf contrast at closer tip-sample distances can also be attributed to the increasingly pronounced lateral relaxations of the probe particle. More interestingly, sharp lines also become visible in the intermolecular regions, Fig. 2(b), where no covalent bonds exist.

The origin of sharp lines in AFM images between atoms is schematically illustrated in Fig. 3 for the example of the DBTH molecule from Ref. [18], for which such a sharp line is observed between two sulfur atoms which are *not* covalently bonded [see Ref. [18] for the experimental image and Fig. 3(b) (inset) for the simulation]. In Fig. 3(a) the simulated repulsive potential and the attractive basins felt by the probe particle above the DBTH molecule in the vicinity of the two nonbonded sulfur atoms are shown in a three-dimensional plot, together with the trajectories of the probe particle as the tip approaches the sample. One clearly observes a repulsive saddle between the two sulfur-derived hillocks [a cross section through this *smooth* saddle is displayed in the bottom diagram of Fig. 3(b)]. The trajectories in Fig. 3(a) reveal that the probe particle relaxes away from the saddle ridge. This means that, e.g., for the tip position x_{tip} in Fig. 3(b) the probe particle is subject to the repulsive force from the sample at x_{probe}. The mapping of forces at x_{probe} to the macroscopic tip coordinate x_{tip} introduces the sharp ridge in the frequency shift signal Δf that is shown in the upper part of Fig. 3(b), although the surface potential V_{Surf} has a smooth saddle.

The mechanism illustrated in Fig. 3 is operational and leads to sharp lines in the images whenever a repulsive saddle occurs in the potential felt by the probe particle. The origin of this saddle can either be the presence of "real" electron density or the close proximity of atoms. In the case of covalent bonds, the electron density also shows up as a smooth feature in AFM images recorded at large tip distances at which the probe particle does not show appreciable relaxation [first column of Figs. 2(a) and 2(b)]. In the other case, the saddle arises merely from the convolution of the electron densities of the probe particle and the neighboring sample atoms at close tip-sample distances and will disappear for larger distances.

Note that at very close distances the molecular contrast in the experimental images may sometimes become significantly asymmetric; see Fig. 2(c). We attribute this observation to an asymmetry of some of the CO tips. To confirm this hypothesis, we have repeated the simulations using a tilted probe, where the equilibrium position of the probe particle is displaced by 1 Å along y axis away from the lateral position of the tip base. The resulting images show asymmetric contrast on benzene rings and in intermolecular features in good agreement with the experimental findings; see Supplemental Material [25], Fig. 4 and Video 1,2.

B. High-resolution STM contrast on and between molecules

We now analyze the high-resolution STM contrast (i.e., STHM and similar atomic probe contrasts) [6–9]. This contrast has two aspects. On molecules their geometric structure becomes visible, similar to high-resolution AFM [11], while between molecules very pronounced intermolecular features, such as sharp lines between oxygen and hydrogen atoms or sharp-edged trapezoids between the perylene and anhydride sides of two PTCDA molecules, appear [8,9]. The first aspect regularly manifests itself very clearly for H_2-, D_2-, and CO-functionalized tips, whereas the latter is more optimally
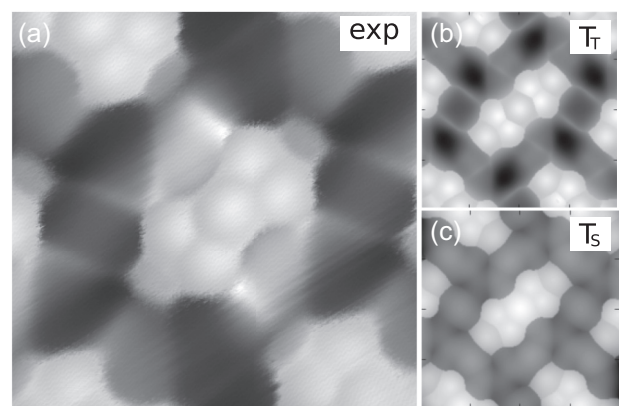

FIG. 4. Intermolecular contrast in high-resolution STM images. (a) Experimental constant height image recorded with a Xe tip over PTCDA/Ag(111). Imaging parameters: area 18 Å × 18 Å; $V = -4$ mV. Prior to the imaging the tip was stabilized at $I = 0.1$ nA and $V = -350$ mV; then the bias was changed to $V = -4$ mV and the tip was moved by 4 Å closer to the surface. (b) Simulated STM image with Xe probe particle (T_T tunneling channel). (c) Simulated STM image with Xe probe particle (T_S tunneling channel). Panels (b) and (c) display approximately the same area as panel (a).

pronounced with H_2, D_2, and Xe tips [9]. As we show now, both aspects of high-resolution STM contrast are closely linked to the same probe particle relaxation that also governs high-resolution AFM images.

First, we focus on the contrast on the molecules, employing exemplary images of PTCDA/Au(111) displayed in Fig. 2(e) that were observed in experiments with a CO-functionalized tip. Using the generic transport model described above, we find that the spatial variation of the tunneling T_S between the probe particle and the sample [Fig. 2(d)] exhibits all essential features of the experimental images in Fig. 2(e). In particular, the overall shape of the molecules and at close distances the appearance of sharp contours between the carbon rings are both reproduced very well. Thus we are led to the conclusion that in this case of a CO tip the experimentally observed high-resolution STM images are mainly determined by the T_S tunneling process.

Turning next to the remarkable STM contrast in the regions between the molecules, we choose the example of a Xe tip (Fig. 4). This time we find excellent agreement between experiment [Fig. 4(a)], carried out on PTCDA/Ag(111), and the simulated image of T_T tunneling [Fig. 4(b)]. Also, the intramolecular contrast (bright aromatic rings with sharp C-C bonds appearing dark) is well reproduced in the T_T channel, although on the molecules the difference between the T_T and T_S images in Fig. 4(b) and Fig. 4(c) is not so large.

Apparently, different experimental situations generate tunneling contrasts of either T_S or T_T type. The obvious questions is why? The variation of the tunneling current in each channel depends exponentially on the distance between the probe particle and the tip base (T_T) or the surface atoms (T_S). In the case of a CO tip, the presence of the stiff covalent bond between CO and the tip base implies only minor changes in the tip-CO distance as the tip is scanned across the sample. Consequently, the T_T channel does not contribute to the STM contrast significantly and the T_S channel prevails.

The situation is different in the case of a Xe tip. The weak interaction (i.e., less stiff bond) between the Xe atom and the tip base leads to more contrast in the T_T channel for Xe than for CO. At the same time, the contrast in the T_S channel will be reduced for Xe relative to CO, for two reasons. First, while CO is electronically more strongly coupled to the tip (i.e., low β) than to the sample, the electronic couplings of the Xe atom to the tip and the sample are expected to be rather comparable; this reduces the relative importance of the coupling to the sample. Secondly and even more importantly, the large atomic radius of Xe smears out the variation of the surface potential, and thus the contrast in T_S, effectively. In conclusion, the mechanically and electronically more weakly coupled part of the junction tends to determine the high-resolution STM image.

C. Can hydrogen bonds be imaged?

The striking AFM/STM contrast between molecules, including the sharp lines observed there, appear suggestive of intermolecular bonds [8,9,16,17,23]. We therefore proceed with addressing in the framework of our mechanical model the imaging of *hydrogen bonds* with AFM that was attributed to
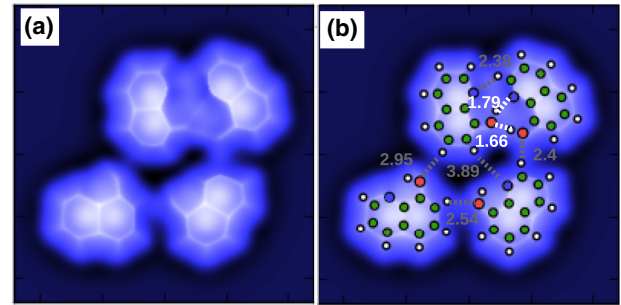

FIG. 5. (Color online) Sharp intermolecular contrast and hydrogen bonds, part I. (a) A simulated AFM image for a 8-hydroxyquinoline tetramer with CO probe particle (tip-sample distance 7.4 Å). The sharp lines in intermolecular regions agree very well with the contrast reported in Fig. 2d of Ref. [17]. (b) Same image as in panel (a), but with a schematic overlay of the molecular structure, with atoms discriminated by colors (white: hydrogen; green: carbon; blue: nitrogen; red: oxygen) and hydrogen bonds (short and strong hydrogen bonds: white; weaker hydrogen bonds: gray). Numbers indicate bond lengths in Å. The image color scale is rescaled by maximum and minimum values of Δf to provide best contrast.

the enhanced electron density between oxygen and hydrogen atoms of neighboring molecules [17].

Our previous discussion of the results displayed in Figs. 2, 3, and 4 has shown quite generally that the intermolecular contrast is very closely related to the lateral relaxation of the probe particle. We are therefore led to the suggestion that also the "hydrogen bonds" of Ref. [17] may in fact be due to this effect. To test this conjecture that the observation of *apparent bonds* is in general mainly driven by the relaxation of the probe particle, we have performed AFM simulations for the 8-hydroxyquinoline tetramer (Fig. 5) that was investigated by Zhang *et al.* [17]. The experimental image depicted in Fig. 2B in Ref. [17] should be directly compared to our simulated image at the distance $z = 7.4$ Å [Fig. 5(a)]. Our simulation resolves sharp intermolecular lines connecting typical donors ($-$OH groups) and acceptors (N, O atoms) of hydrogen bonds very well (Fig. 5). According to the mechanism discussed in the context with Fig. 3, these lines are well resolved in our model simply because of the close proximity between donor and acceptor atoms [see white dotted lines in Fig. 5(b) with bond length labels]. Certainly, our purely mechanical model does not have an increased electron density along those lines. On the basis of this finding we suggest that also in the experiments of Zhang *et al.* [17] probe particle relaxation may in fact be the origin of the observed features which the authors identify with hydrogen bonds.

The longer hydrogen bonds between CH groups and O, N atoms [gray dotted lines, Fig. 5(b)], which are less pronounced in Fig. 2B of Ref. [17], become visible in our simulations only at even closer tip-sample proximity (cf. Supplemental Material [25], Fig. 6). This as well as some other minor discrepancies with experimental image (namely the different distortion of aromatic rings) can be explained naturally by two reasons. Firstly, the positions of the atoms in the molecules in our input geometry are probably not exactly the same as in experiment. Secondly, in the experiments, the molecules can move slightly on the surface in both lateral and vertical direction under forces
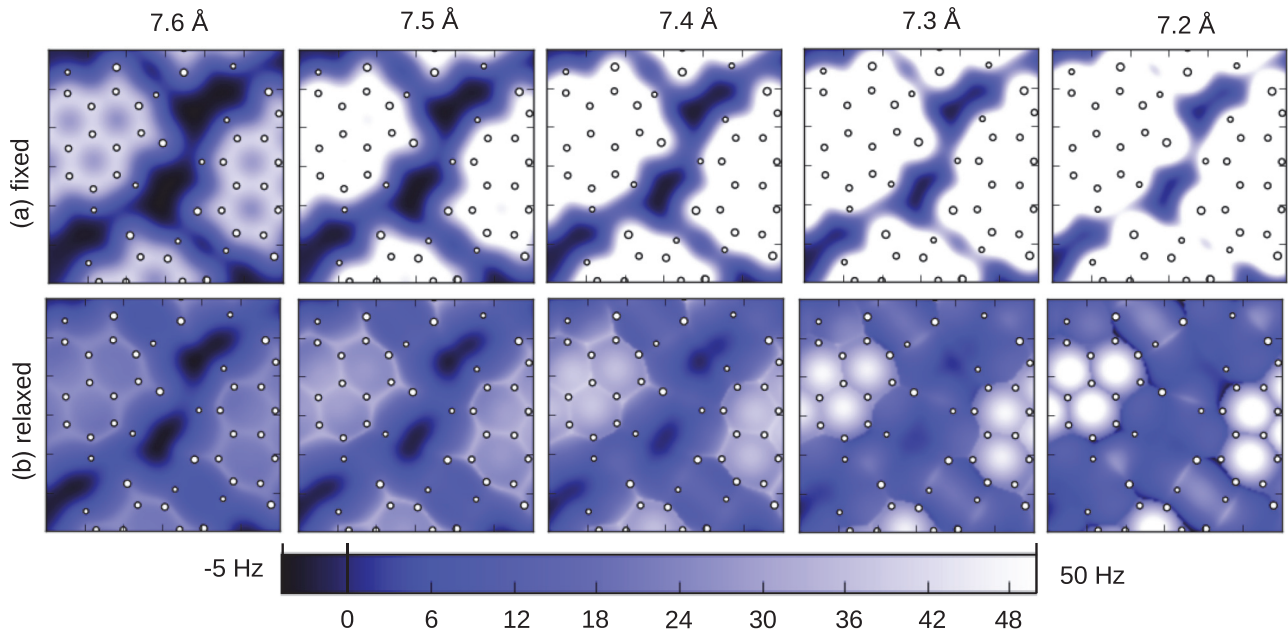
FIG. 6. (Color online) Sharp intermolecular contrast and hydrogen bonds, part II. Simulated AFM images of a monolayer of naphthalene tetracarboxylic diimide (NTCDI) molecules that was studied experimentally by Sweetman *et al.* in Ref. [23]. (a) Without probe particle relaxation; (b) with probe particle relaxation. The images in panel (b) agree very well with experimental AFM images in Figs. 1b and 1c of Ref. [23].

exerted by the tip. These degrees of freedom are not included in our simulation.

Recently an alternative explanation of the origin of the hydrogen bonds was proposed by Sweetman *et al.* [23]. They attribute the imaging mechanism of the hydrogen bonds to a change of the electron density upon tip approach, but without considering image distortions due to tip relaxation. Here we show that although the mechanism discussed in Ref. [23] may be present, it is the probe relaxation which is the driving mechanism that makes the intermolecular bonds visible in the AFM experiment. To do so, we compare experimental AFM images acquired over naphthalene tetracarboxylic diimide (NTCDI) [23] to images that were calculated using our AFM model without [Fig. 6(a)] and with [Fig. 6(b)] probe particle relaxation. Although in both cases we observe an increased repulsion in the region between oxygen and hydrogen atom, only the results obtained with the relaxing probe particle resemble the experimental evidence in Ref. [23]. In simulated images for the fixed probe particle the variation of the repulsion over the bond is very smooth (similar to what is shown in Fig. 4f of Ref. [23]) and the magnitude of the repulsive interaction over hydrogen bonds is much smaller than over the molecule. Only if we take the probe particle relaxation into account are we able to reproduce the sharp contrast visible simultaneously over the molecules and over the intermolecular region in the experiment.

In addition, we note that the observation of an enhanced Pauli repulsion over the area of the hydrogen bond (i.e., between the oxygen and hydrogen atoms of neighboring molecules) in calculations with a rigid probe particle need not be related to an increased electron density in this area. A similar effect is caused by the convolution process due to

the finite size of the probe particle, as the following simple consideration shows. For the purpose of the present argument, the Pauli repulsion can be approximated by the overlap of the electron densities of the tip and the sample. Even in the case when there is no electronic density between two atoms on the surface, e.g., the oxygen and hydrogen atoms in a hydrogen bond, a probe particle with a radius that is comparable to the oxygen hydrogen distance will overlap with both surface atoms simultaneously. In AFM imaging, this gives rise to the enhanced repulsion in between the atoms, as a mere consequence of the superposition of the repulsions stemming from both surface atoms. Therefore, it is hard to discriminate the mechanism proposed in Ref. [23] from this straightforward convolution effect that will always be present.

IV. CONCLUSIONS

In conclusion, we have developed a reliable numerical model which despite its simplicity is able to reproduce high-resolution AFM and STM images of molecules, recorded with functionalized tips, very well. The excellent agreement between simulated and experimental images allows us to show that the appearance of sharply resolved structural resolution, observed experimentally both in the AFM and the STM mode, is due to strong lateral relaxations of the probe particle attached to the metallic tip apex. At close tip-sample distances these relaxations follow the potential energy basins produced by the Pauli repulsion. Therefore, sharp features appearing in the images always coincide with the borders of neighboring basins, i.e., the narrow areas where the magnitude and the direction of the lateral relaxation of the probe particle changes strongly upon small variations of the position of the tip relative to the

sample. Since the lateral and the vertical relaxations of the probe particle are closely coupled, in the area between the neighboring basins the vertical position of the probe particle also becomes very sensitive to the precise position of the tip, thus producing the sharp image features in the AFM images.

Furthermore, we have also demonstrated that our mechanical model, if combined with a generic model of tunneling through the probe particle junction based on the simplified Landauer formalism, successfully explains the features of high-resolution atomic contrast of STHM. Regarding the STM contrast, we note a few salient points. (1) Any extension of the present tunneling model that includes more realistic charge transport effects will not change its essential feature: namely, that the observed STM contrast is directly related to the relaxation of the probe particle. (2) Our model confirms the concept of the probe particle acting as a combined sensor and transducer [7–9]. This concept relies on the presence of at least one internal degree of freedom in the tunneling junction which can sense a certain physical quantity and transduce this signal into another physical quantity. In the present case, our mechanical model shows how the probe particle senses repulsive forces and by its response to them (mainly lateral relaxation) couples this signal into the tunneling conductance of the junction. (3) The high-resolution AFM and STM imaging mechanism discussed in this paper can be also applied to point contact microscopy [32–34] and contact force microscopy [35,36], as in all the cases sharp features originate

from relaxation of the central part of the junction. However, in the present case there is *no hysteresis* in the position of the probe particle as the tip is scanned across the surface. As a consequence, there is also no dependence on scanning direction or speed, and all images can be reconstructed from force vs distance or conductance vs distance curves measured "statically" (as far as the lateral position is concerned) on a grid above the surface.

Finally, we have demonstrated that most sharp image features recorded with functionalized STM/AFM tips, and in particular the resolution obtained in the areas between molecules, do not follow necessarily an increased electron density corresponding to any kind of interatomic or intermolecular bonds, but they trace the sharp boundaries between basins of the short-range repulsive potential produced by atoms that reside close to each other.

ACKNOWLEDGMENTS

[1] G. Binnig, H. Rohrer, C. Gerber, and E. Weibel, Phys. Rev. Lett. **49**, 57 (1982).

[2] G. Binnig, C. F. Quate, and C. Gerber, Phys. Rev. Lett. **56**, 930 (1986).

[3] J. Repp, G. Meyer, S. M. Stojkovic, A. Gourdon, and C. Joachim, Phys. Rev. Lett. **94**, 026803 (2005).

[4] L. Bartels, G. Meyer, K.-H. Rieder, D. Velic, E. Knoesel, A. Hotzel, M. Wolf, and G. Ertl, Phys. Rev. Lett. **80**, 2004 (1998).

[5] L. Gross, N. Moll, F. Mohn, A. Curioni, G. Meyer, F. Hanke, and M. Persson, Phys. Rev. Lett. **107**, 086101 (2011).

[6] R. Temirov, S. Soubatch, O. Neucheva, A. C. Lassise, and F. S. Tautz, New J. Phys. **10**, 053012 (2008).

[7] C. Weiss, C. Wagner, C. Kleimann, M. Rohlfing, F. S. Tautz, and R. Temirov, Phys. Rev. Lett. **105**, 086103 (2010).

[8] G. Kichin, C. Weiss, C. Wagner, F. S. Tautz, and R. Temirov, J. Am. Chem. Soc. **133**, 16847 (2011).

[9] G. Kichin, C. Wagner, F. S. Tautz, and R. Temirov, Phys. Rev. B **87**, 081408 (2013).

[10] F. Giessibl, Rev. Mod. Phys. **75**, 949 (2003).

[11] L. Gross, F. Mohn, N. Moll, P. Liljeroth, and G. Meyer, Science **325**, 1110 (2009).

[12] L. Gross, F. Mohn, N. Moll, B. Schuler, A. Criado, E. Guitián, D. Peña, A. Gourdon, and G. Meyer, Science **337**, 1326 (2012).

[13] N. Moll, L. Gross, F. Mohn, A. Curioni, and G. Meyer, New J. Phys. **12**, 125020 (2010).

[14] M. P. Boneschanscher, S. K. Hämäläinen, P. Liljeroth, and I. Swart, ACS Nano **8**, 3006 (2010).

[15] M. Neu, N. Moll, L. Gross, G. Meyer, F. J. Giessibl, and J. Repp, Phys. Rev. B **89**, 205407 (2014).

[16] C. Weiss, C. Wagner, R. Temirov, and F. S. Tautz, J. Am. Chem. Soc. **132**, 11864 (2010).

[17] J. Zhang, P. Chen, B. Yuan, W. Ji, Z. Cheng, and X. Qiu, Science **342**, 611 (2013).

[18] N. Pavlíček, C. Herranz-Lancho, B. Fleury, M. Neu, J. Niedenführ, M. Ruben, and J. Repp, Phys. Status Solidi B **250**, 2424 (2013).

[19] L. Kilian, E. Umbach, and M. Sokolowski, Surf. Sci. **600**, 2633 (2006).

[20] G. Mercurio, O. Bauer, M. Willenbockel, N. Fairley, W. Reckien, C. H. Schmitz, B. Fiedler, S. Soubatch, T. Bredow, M. Sokolowski, and F. S. Tautz, Phys. Rev. B **87**, 045421 (2013).

[21] P. Jelínek, H. Wang, J. P. Lewis, O. F. Sankey, and J. Ortega, Phys. Rev. B **71**, 235101 (2005).

[22] J. P. Lewis, P. Jelínek, J. Ortega, A. A. Demkov, D. G. Trabada, B. Haycock, H. Wang, G. Adams, J. K. Tomfohr, E. Abad, H. Wang, and D. A. Drabold, Phys. Status Solidi B **248**, 1989 (2011).

[23] A. M. Sweetman, S. P. Jarvis, H. Sang, I. Lekkas, P. Rahe, Y. Wang, J. Wang, N. R. Champness, L. Kantorovich, and P. Moriarty, Nat. Commun. **5**, 3931 (2014).

[24] W. L. Jorgensen and J. Tirado-Rives, J. Am. Chem. Soc. **110**, 1657 (1988).

[25] See Supplemental Material at http://link.aps.org/supplemental/10.1103/PhysRevB.90.085421 for (i) additional figures regarding the robustness of the model, the influence of tip asymmetry and orbital symmetries on the simulated images, and the imaging of hydrogen bonds, (ii) for more details on the simulation method, and (iii) for two videos showing the evolution of simulated AFM images as the tip approaches the surface.

[26] F. Mohn, B. Schuler, L. Gross, and G. Meyer, Appl. Phys. Lett. **102**, 073109 (2013).

[27] F. Mohn, J. Repp, L. Gross, G. Meyer, M. S. Dyer, and M. Persson, Phys. Rev. Lett. **105**, 266102 (2010).

[28] J. E. Sader and S. P. Jarvis, Appl. Phys. Lett. **84**, 1801 (2004).

[29] R. Landauer, IBM J. Res. Dev. **1**, 223 (1957).

[30] M. Rohlfing, R. Temirov, and F. S. Tautz, Phys. Rev. B **76**, 115421 (2007).

[31] P. Jelínek, M. Ondráček, and F. Flores, J. Phys.: Condens. Matter **24**, 084001 (2012).

[32] J. A. Stroscio and R. J. Celotta, Science **306**, 242 (2004).

[33] Y.-H. Zhang, P. Wahl, and K. Kern, Nano Lett. **11**, 3838 (2011).

[34] G. Schull, Y. J. Dappe, C. González, H. Bulou, and R. Berndt, Nano Lett. **11**, 3142 (2011).

[35] H. Hölscher, U. D. Schwarz, O. Zwörner, and R. Wiesendanger, Phys. Rev. B **57**, 2477 (1998).

[36] H. Hölscher, U. Schwarz, and R. Wiesendanger, Europhys. Lett. **36**, 19 (1996).